Original article

Institution of MECHANICAL ENGINEERS

Journal of MATERIALS: DESIGN AND APPLICATIONS

Macro-scale finite element simulation of wire-arc additive manufacturing

Proc IMechE Part L:
J Materials: Design and Applications
2025, Vol. 239(5) 1013–1022

DOI: 10.1177/14644207241272840
journals.sagepub.com/home/pil
Sage

JPM Pragana[1], RFV Sampaio[1], IMF Bragança[2], CMA Silva[1], CV Nielsen[3] and PAF Martins[1]

Abstract

This paper focuses on the development of a finite element computer software to perform macro-scale thermo-mechanical simulations of wire-arc additive manufacturing (WAAM). The emphasis is placed on various aspects of computer implementation, such as modeling the heat source, incorporating an element birth approach to replicate material deposition, and ensuring compatibility of solution time increments with the wire feed rate, travel speed of the heat source and melt pool volume. Thermal strains are also included due to their impact on residual stresses and distortions of the built parts after finishing material deposition. Experiments consisting of single bead, multi-layer deposition of AISI 316L stainless steel along linear paths are utilized to validate the predicted temperature distribution over time and evaluate the computed geometry and distortions of the deposited vertical walls after unclamping. Microstructure observations of samples extracted from the walls combined with finite element estimates of the temperature gradient help understand the influence of temperature history on the morphology and orientation of columnar grain growth.

Keywords

Wire-arc additive manufacturing, macro-scale modelling, finite element method, experimentation, stainless steel

Date received: 26 June 2024; accepted: 26 July 2024

Introduction

Wire-arc additive manufacturing (WAAM) is a form of wire-direct energy deposition (wire-DED) that utilizes gas metal arc, gas tungsten arc, or plasma arc as heat sources and shares working principles with well-established arc welding processes.[1] Numerical modelling of WAAM can be conducted across three different scales: macro, meso, and micro (Figure 1). At macro-scale (Figure 1(a)), the description is conducted through thermo-mechanical coupled approaches, which discretize the filler and base materials by means of finite elements and replace the torch and electric arc with a moving heat source model.[2]

At the meso-scale (Figure 1(b)), the modeling lengths range from micrometers to millimeters, focusing not on replicating the deposition of material along a specific path to obtain the built part, but rather on capturing the interaction between the electric arc and the filler and base materials. The aim is on simulating the heat transferred to the filler material droplets within the electric arc, understanding the mechanisms of their formation, detachment, and impingement into the molten pool,[3] and analyzing the influence of gas flow rate on the incidence of porosity.[4] This is generally carried out through complex multiphysics modelling approaches that couple the governing equations of heat transfer, solid mechanics, and fluid dynamics.

Micro-scale modelling is generally linked to a specific location of a built part, which acts as a representative volume element (RVE) (Figure 1(c)) for simulating phase transformations and microstructure formation.[5] Phase field thermodynamic-based models for solving interfacial problems,[6] as well as Monte Carlo and cellular automata randomness computational algorithms,[7] are commonly used to simulate solidification, grain growth and phase transformations in the deposited material.

Due to the necessity of exchanging information between macro and micro-scale models bidirectionally to solve the thermal cycle of the built part while capturing the evolution of its microstructure, the use of RVE's imposes significant limitations on modelling real

[1]IDMEC, Instituto Superior Técnico, Universidade de Lisboa, Portugal
[2]CIMOSM, Instituto Superior de Engenharia de Lisboa, Instituto Politécnico de Lisboa, Portugal
[3]Department of Civil and Mechanical Engineering, Technical University of Denmark, Denmark

Corresponding author:
PAF Martins, IDMEC, Instituto Superior Técnico, Universidade de Lisboa, Portugal.
Email: pmartins@tecnico.ulisboa.pt

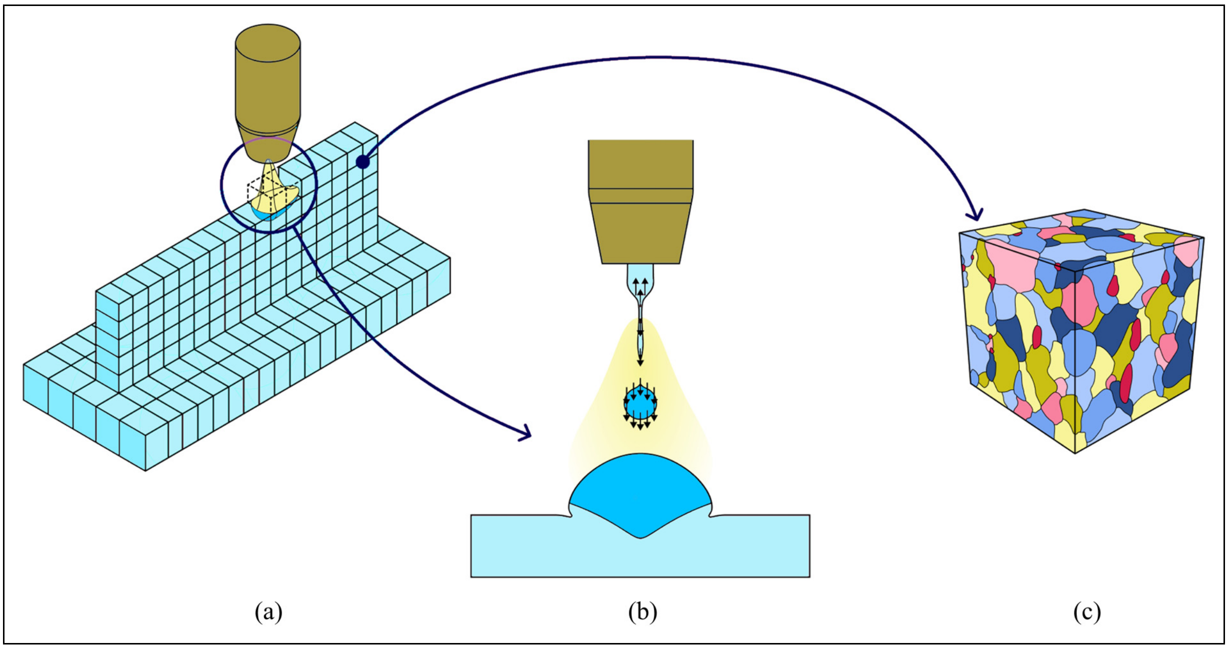

Figure 1. Modelling of wire-arc additive manufacturing at (a) macro, (b) meso and (c) micro scales.

timescales of WAAM. A similar difficulty exists with the lengths and timescales of meso-scale modelling, which are notably smaller compared to those of the built parts at the macro-scale level.

The abovementioned difficulties limit the applicability of multi-scale modelling, as the exchange of information between macro, meso, and micro-scale phenomena leads to ambitious numerical problems with demanding CPU requirements.[8] This justifies the interest in macro-scale modeling for WAAM, drawing from prior work in computational welding from the late 1980s and 1990s comprehensively reviewed in reference.[9]

Recent advancements in macro-scale modeling of WAAM demonstrate its effectiveness in estimating the temperature history over time, predicting cooling rates and their impact on solidification and microstructure formation, as well as in determining residual stresses and distortions of the built parts.[10]

This paper presents the main ingredients the authors considered in developing an in-house thermo-mechanical finite element software to perform macro-scale modeling of WAAM. Emphasis is placed on modeling the heat source, incorporating an element birth approach, ensuring compatibility of solution time increments with deposition parameters and melt pool volume, accounting for the thermal stresses, and predicting the temperature gradients during material deposition. These developments are supported by comprehensive experiments involving single bead, multi-layer deposition of AISI 316L stainless steel along linear paths to create vertical walls, which are designed to assess the computed temperature distribution over time and distortions after unclamping, ensuring the validity and reliability of software development.

Temperature gradients are determined by means of an innovative procedure performed directly at finite element level and microstructure observations of samples extracted from the walls are utilized to compare the predicted temperature gradients with the morphology and orientation of columnar grain growth.

Finite element modelling

Governing equations

Macro-scale finite element modelling of WAAM involves solving the heat transfer equation,

$$k\nabla^2 T - \rho c \frac{\partial T}{\partial t} + \dot{q} = 0 \tag{1}$$

where k represents the thermal conductivity, ρ stands for the density, c denotes the specific heat capacity, and $\dot{q}$ is the total input power density, in combination with the quasi-static equilibrium equations in the current configuration, under the absence of body forces,

$$\frac{\partial \sigma_{ij}}{\partial x_j} = 0 \tag{2}$$

In the above equation, σ_{ij} represents the Cauchy stress tensor, and x_j denotes an arbitrary position within the baseplate and deposited material at the current instant of time.

The finite element solution of the governing equations utilizes integral forms that instead of satisfying the heat transfer and static equilibrium equations exactly (that is, pointwise), only fulfill them in an average sense over the entire volume. The integral form of the heat transfer equation (1) can be written as,

$$\int_V k\nabla T\nabla(\delta T)dV + \int_V \rho c\frac{dT}{dt}\delta T dV - \int_{S_q} q_n \delta T dS_q - \int_V \dot{q}\delta T dV = 0 \qquad (3)$$

where, the symbol δT represents an arbitrary variation in the temperature, and $q_n = k\nabla T \cdot n$ denotes the heat flux along the surface S_q (which belongs to the closed surface S of the baseplate and deposited material), with n representing the vector of direction cosines of the normal to the surface S_q. Additionally, $\dot{q}$ represents the power density transferred from the heat source to the baseplate and deposited material.

On the other hand, the integral form of the quasi-static equilibrium equations (2) is expressed by,

$$\int_V \sigma_{ij}\frac{\partial(\delta u_i)}{\partial x_j}dV - \int_{S_t} t_i \delta u_i dS = 0 \qquad (4)$$

where δu_i represents an arbitrary variation in the displacement (or velocity), and $t_i = \sigma_{ij}n_j$ denotes the tractions applied on the boundary S_t with the prescribed traction having the unit normal vector n_j. The duality between velocity and displacement arises from whether the finite element implementation is done in the rate-form or not.

Computer implementation

Heat source. Asymmetric Gaussian distributed heat source models such as the moving double-ellipsoid (Figure 2(a)) proposed by Goldak et al.,[11] are commonly used in finite element analysis of WAAM,[12] as they effectively account for the total power $\dot{Q}$ transferred to both filler and base materials.[13]

The double-ellipsoid heat source model is characterized by two geometric parameters representing the half-width b and depth d of the molten pool along with two additional parameters defining the maximum distances a_f and a_r between the broadest spots of the pool to the molten front (x-positive) and rear (or, solidification front, x -negative). The values of the half-width b and depth d of the molten pool can typically be derived from a cross-section of the deposited material and assumed as $a_f \cong 0.5b$ and $a_r \cong 2b$, in the absence of experimental data.[11]

The total power density $\dot{q}$ supplied by the double-ellipsoid heat source model is expressed by means of the following asymmetric Gaussian distribution,

$$\dot{q} = \frac{6\sqrt{3}\dot{Q}f_{f,r}}{\pi\sqrt{\pi}a_{f,r}bd}exp\left\{-3\left(\frac{x^2}{a_{f,r}^2}+\frac{y^2}{b^2}+\frac{z^2}{d^2}\right)\right\} \qquad (5)$$

where, $\dot{Q} = \eta UI$ represents the total input power of the heat source, η denotes the arc efficiency, U stands for the voltage and I is the electric current. The factors f_f and f_r are the fractions of power transferred to the front and rear, with $f_f + f_r = 2$.

Discretization by finite elements. The computer implementation of the thermo-mechanical governing equations of WAAM in the finite element software i-form developed by the authors[14] is accomplished through discretization of the wall into M three-dimensional hexahedral elements. Assuming temperature $T = N^T T$ to be interpolated by means of shape functions within each element m, the integral form of the heat transfer equations can be expressed in matrix form at the elemental level as follows,

$$\sum_{m=1}^{M}\left\{\int_{V^m} k\mathbf{M}\mathbf{M}^{\mathrm{T}}\mathbf{T}dV^m + \int_{V^m}\rho c\mathbf{N}\mathbf{N}^{\mathrm{T}}\dot{\mathbf{T}}dV^m - \int_{S_q^m} q_n\mathbf{N}dS_q^m - \int_{V^m}\dot{q}_b\mathbf{N}dV^m\right\} = 0 \qquad (6)$$

where N denotes the matrix containing the shape functions and $M = \nabla N$ represents a matrix built from the gradient operator. Alternatively, the system of equations resulting from (6) can be abbreviated as follows,

$$\mathbf{KT} + \mathbf{C}\dot{\mathbf{T}} = \mathbf{Q} \qquad (7)$$

where $\mathbf{K}$ represents the heat conduction matrix, $\mathbf{C}$ denotes the heat capacity matrix and $\mathbf{Q}$ is the heat flux vector, which accounts for the power density $\dot{q}$ transferred to the filler and base materials, along with the heat dissipation through radiation and convection to the environment.

Following the strategy proposed by Montevecchi et al.,[2] which splits the total input power $\dot{Q}$ of the heat source into two components - power supplied to the filler $\dot{Q}_f$ and base $\dot{Q}_b$ materials (Figure 2(b)) – the heat flux vector $\mathbf{Q}$ in (7) is formulated to account only for the power density $\dot{q}_b$ transferred from the heat source to the base material. The power density $\dot{q}_f$ supplied to the filler,

$$\dot{q}_f = \frac{\dot{Q}_f}{V_{el}} \qquad (8)$$

is assigned to a box with length l, width w and height h (i.e., with a volume $V_{el} = lwh$) that represents the currently heated filler material being deposited at the current instant of time.

In what concerns the mechanical model, the computer implementation of the integral form of the quasi-static equilibrium equations with appropriate constitutive equations for temperature-dependent elastic-plastic materials is expressed by the following matrix set of non-linear equations,

$$\mathbf{Ku} = \mathbf{F} \qquad (9)$$

where $\mathbf{K}$ is the stiffness matrix and $\mathbf{F}$ is the generalized force vector resulting from applied forces, pressure, and thermal loads. The latter are induced by temperature changes within a time increment Δt and are included in

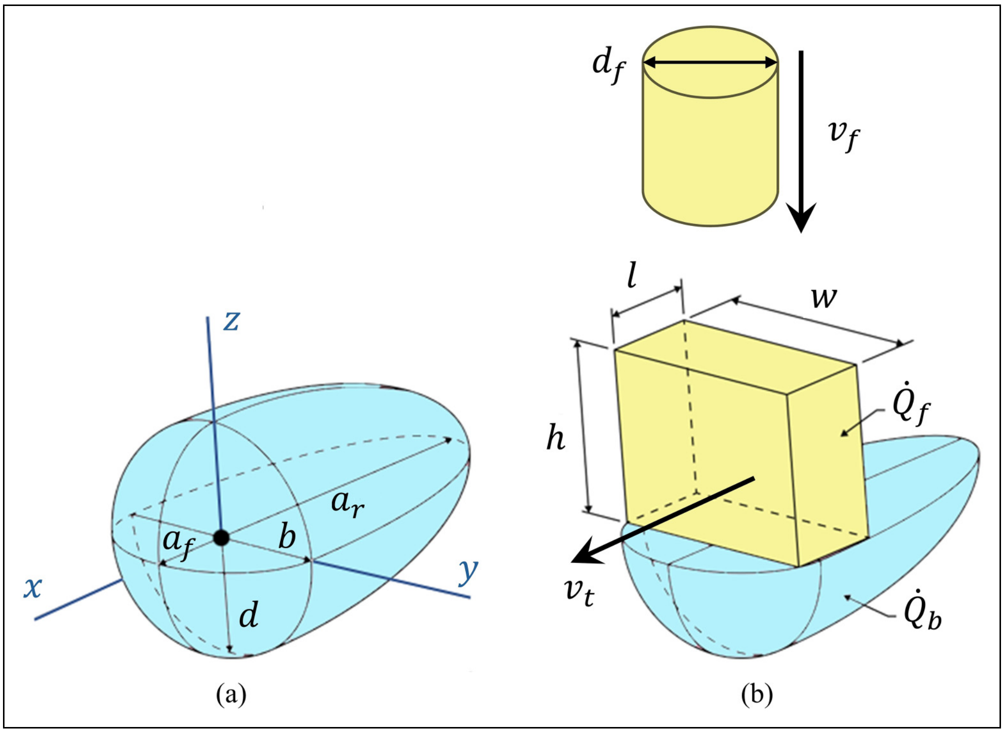

Figure 2. (a) The double ellipsoid heat source model and (b) schematic representation of the compatibility between the wire feed rate v_f and travel speed v_t with the split of the total power $\dot{Q}$ supplied by the heat source into the filler $\dot{Q}_f$ and base $\dot{Q}_b$ materials.

F because of the thermal strain increment $\Delta\varepsilon^t$,

$$\Delta\varepsilon^t = \alpha(T)\Delta T \tag{10}$$

where the symbol α denotes the coefficient of thermal expansion. The thermal strain increment $\Delta\varepsilon^t$ (10) is combined with the elastic strain increment $\Delta\varepsilon^e$, calculated from the elasticity modulus and Poisson ratio, and the plastic strain increment $\Delta\varepsilon^p$ determined from the material flow curve, to obtain the total increment of strain $\Delta\varepsilon = \Delta\varepsilon^e + \Delta\varepsilon^p + \Delta\varepsilon^t$.

The displacement (or, velocity) vector u resulting from the solution of the non-linear set of equations (9) at the end of material deposition by WAAM is typically accountable for the undesirable distortions of the built parts that are caused by the distribution of residual stresses in equilibrium after unclamping, through the constitutive equation,

$$\sigma_{ij} = C_{ijkl}(\varepsilon_{kl} - \varepsilon^p_{kl} - \varepsilon^t_{kl}) \tag{11}$$

where the symbol C_{ijkl} denotes the fourth order material stiffness tensor.

Computational procedure for material deposition. The box lwh in Figure 2(b) consists of new mesh elements that are gradually activated as the heat source moves, simulating the formation, detachment, and impingement of droplets from the filler material into the molten pool. This computational procedure is commonly known as the 'element birth approach', and in the current finite element implementation, a variant named 'born-dead elements' was utilized.

In this variant, the elements defining the successive layers to be deposited during the simulation are initially excluded from the mesh and incorporated into the existing mesh as newborn elements as material is deposited.[15,16] The power density $\dot{q}_f$ supplied to the filler material (8) is converted and delivered at a prescribed temperature T_f to the box lwh, replicating a droplet (Figure 2(b)), following the work of other authors.[17]

Another crucial aspect in the modelling of material deposition is the compatibility between the wire feed rate v_f and the travel speed v_t (Figure 2(b)) of the heat source. Considering the time increment $\Delta t = l / v_t$ for deploying the new mesh elements inside the box lwh, the relation between v_f and v_t must ensure conservation of mass within the filler material,[18]

$$v_t = \frac{\pi d_f^2}{4wh} v_f \tag{12}$$

In the above equation, wh represents the cross section of the box and d_f is the diameter of the wire feedstock.

Experimentation

Deposited material

The experiments in WAAM were carried out utilizing an ESAB Luc Aristo 400 gas metal arc welding power source in conjunction with a 3-axis CNC router table. AISI 316L stainless steel wire feedstock, with a diameter of 1.0 mm, was supplied through the welding torch and melted using a spray transfer mode onto hot rolled AISI 316L baseplates.

The spray transfer mode was chosen to obtain high deposition rates and avoid potential cold lapping defects at the interface between the deposited material and the cold baseplates. To prevent excessive distortion, the baseplates were 15 mm thick and fixed to the table with clamps.

The deposition strategy involved single-bead, twenty-layer deposition sequences along straight linear paths to create vertical walls on the baseplates (also known as the 'substrate'). The beads had a cross-section of 5 mm by 1.26 mm and were deposited using a zigzag strategy, with a waiting time of 30 s between subsequent layers to allow the heat to distribute into the baseplate. The main deposition parameters are summarized in Table 1, and their values were retrieved from a previous work by the authors.[19] The table also includes a deposition scheme and a photograph of a cross-section of a deposited wall.

Finite element modeling of WAAM required accounting for the temperature dependency of the mechanical and physical properties of the AISI 316L stainless steel. The flow stress (true stress vs. true strain response) at various temperatures was obtained from the literature,[20] while the remaining mechanical and physical properties such as the elastic modulus, coefficient of thermal expansion α, thermal conductivity k and heat capacity ρc were sourced from publicly available databases.[21] Figure 3 illustrates the dependency of flow stress and two selected physical properties on temperature.

Methods and procedures

The temperature evolution over time was monitored using a FLIR E86 infrared thermal camera with thermal imaging software for high-resolution image management and analysis. Figure 4 presents a scheme of the vertical wall with the position of two virtual infrared thermocouples, labeled IR1 and IR10, that were set up directly from the thermal imaging software. These virtual infrared thermocouples allowed obtaining the evolution of temperature over time at the center of the first and tenth deposited layers during deposition, cooling, and reheating by subsequent deposition.

In addition, three type-K thermocouples from OMEGA with a wire diameter of 0.38 mm (CHAL-015) were strategically placed inside the baseplate to provide an evolution of temperature over time at predefined locations (refer to labels TC1, TC2 and TC3 in Figure 4). Data from the type-K thermocouples was acquired using a National Instruments NI 9211 thermocouple module (labelled as 'DAQ') connected to a PC, with a sampling rate of 4 Hz.

A cork insulation base was used to prevent heat exchanges between the baseplate and the table.

After deposition, the baseplates were unclamped from the table, and distortions were measured using a TESA Microhite 3D coordinate measuring machine (CMM) probing the longitudinal edges of the bottom surface of the baseplate (corresponding to $z = 0$) with a measuring head diameter of 2 mm.

Subsequently, the deposited walls were cut into different metallurgical test samples by water jet to analyze the microstructure and the influence of temperature gradients on grain morphology and orientation.

Results and discussion

Temperature distribution

The solution of the heat transfer and quasi-static finite element equations (7) and (9) was carried out in a staggered manner, decoupling the thermo-mechanical problem into two sub-problems that are solved sequentially within a time increment Δt. The baseplates and vertical walls were discretized using approximately 25,000 hexahedral elements, with mechanical and physical properties of the material assumed to be temperature dependent as described in Section 3.1 (Figure 5(a)).

The baseplates were clamped to a table to minimize distortion during WAAM, and the clamps were included

Table 1. Summary of the material deposition parameters by WAAM.

Voltage	Current	Wire feed speed	Stick-out length	Travel speed	Gas flow rate (99% Argon)
16.5 V	100 A	6 m/min	10 mm	600 mm/min	10 l/min

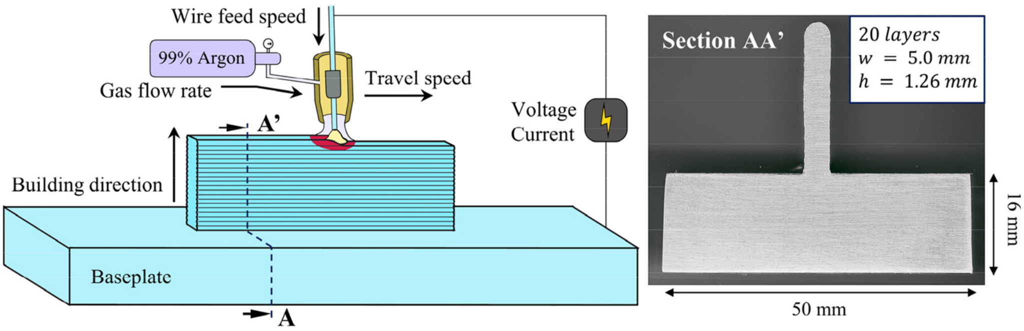

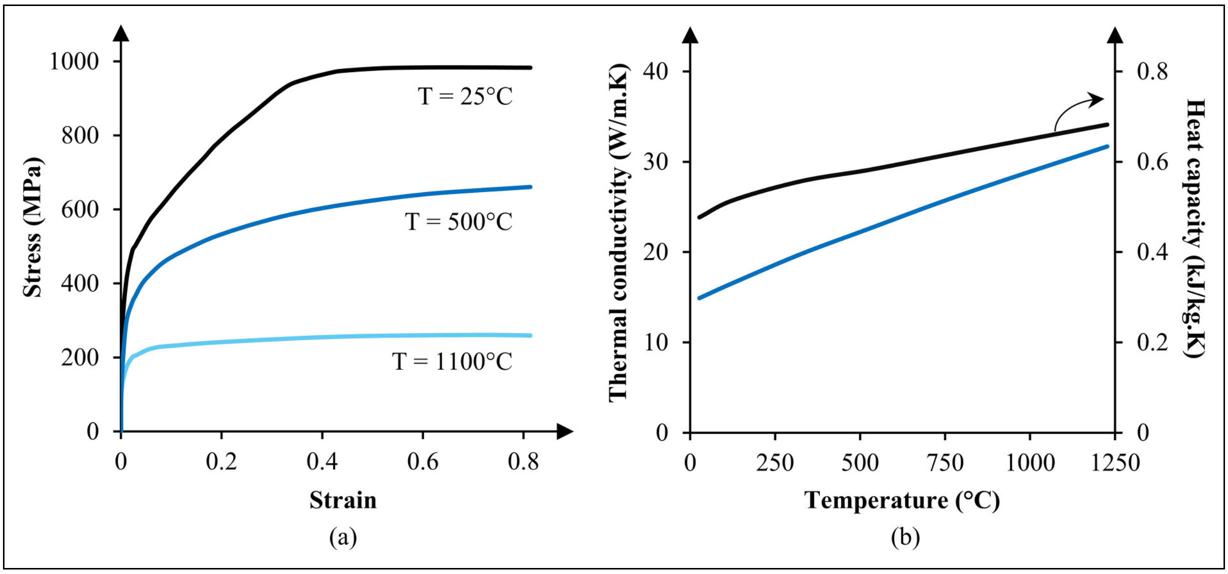

Figure 3. Temperature dependency of AISI 306L stainless steel properties. (a) Flow stress (true stress vs. true strain), (b) thermal conductivity and heat capacity for different temperatures. Note: data to construct the graphics was retrieved from references[20] and [21].

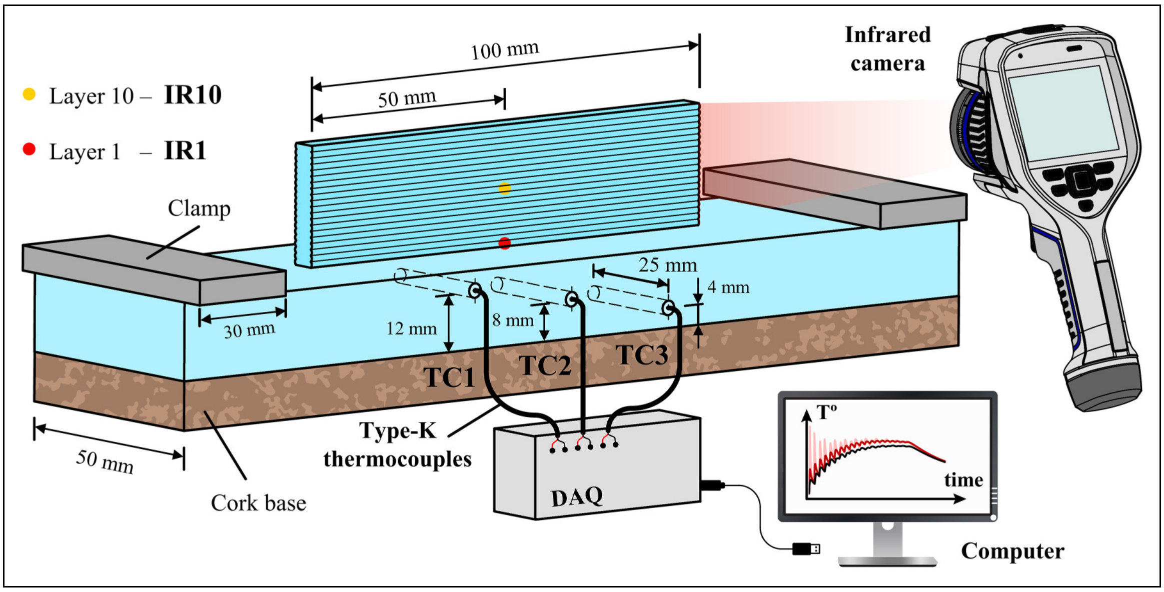

Figure 4. Schematic representation showing the baseplate, the cork insulation base, the vertical wall, the clamps, the infrared thermal camera and the position of the two types of thermocouples.

in the finite element model by means of single node constrains of the left and right bottom surface edges of the baseplates. The remaining surfaces of the models were assigned with free convection boundary conditions with convection coefficient values equal to 15 (W/m^2K) and radiation to the environment.

Figures 5(b) and 5(c) show the finite element predicted and experimentally measured distribution of temperature at two different instants of material deposition. The agreement is good, and the temperature legends in both figures are capped at the melting temperature (approximately equal to 1400˚C) to facilitate the identification of the molten pool. The remaining temperature values provide contours that gradually increase at the front and rear of the molten pool, in agreement with the asymmetric Gaussian distribution of heat flux.

Figure 6 shows the temperature history for two selected points located at the positions of thermocouples TC1 and TC3 (refer to Figure 4). The initial temperature spikes are a direct result of the heat flux distribution, which travels down the centerline and passes near the thermocouples located inside the baseplate during the deposition of the first layer.

The first temperature spike at IR1 results from the addition of filler material to the molten pool during the deposition of the first layer. This experimental spike is

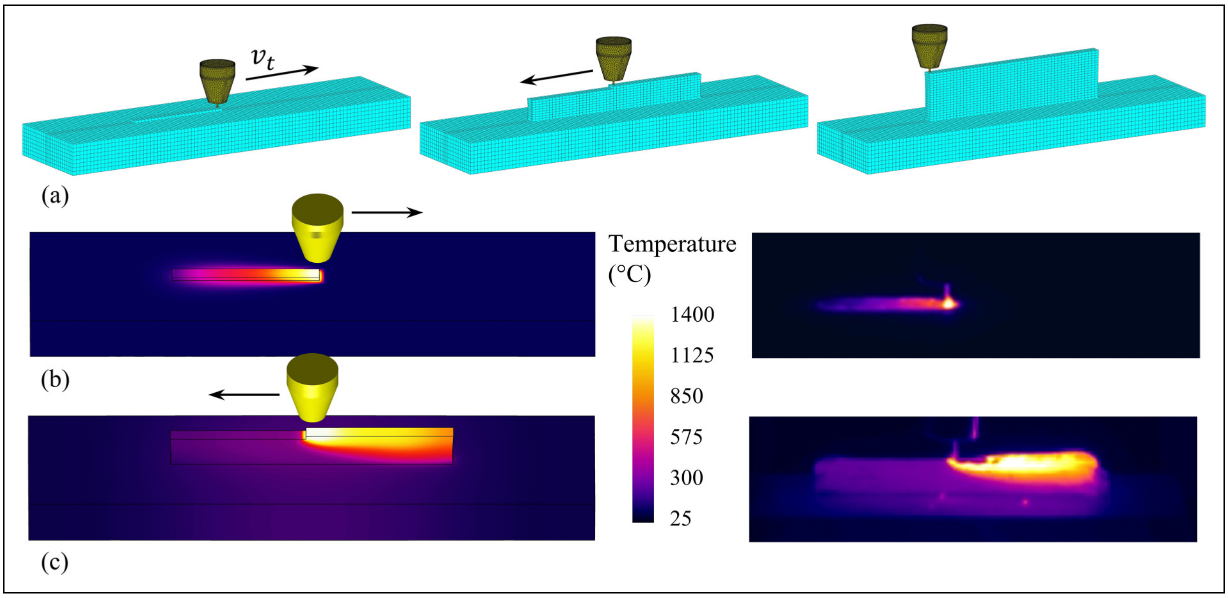

Figure 5. (a) Finite element model with (b) predicted and (c) experimentally measured distribution of temperature during deposition of the first and tenth layers of the wall.

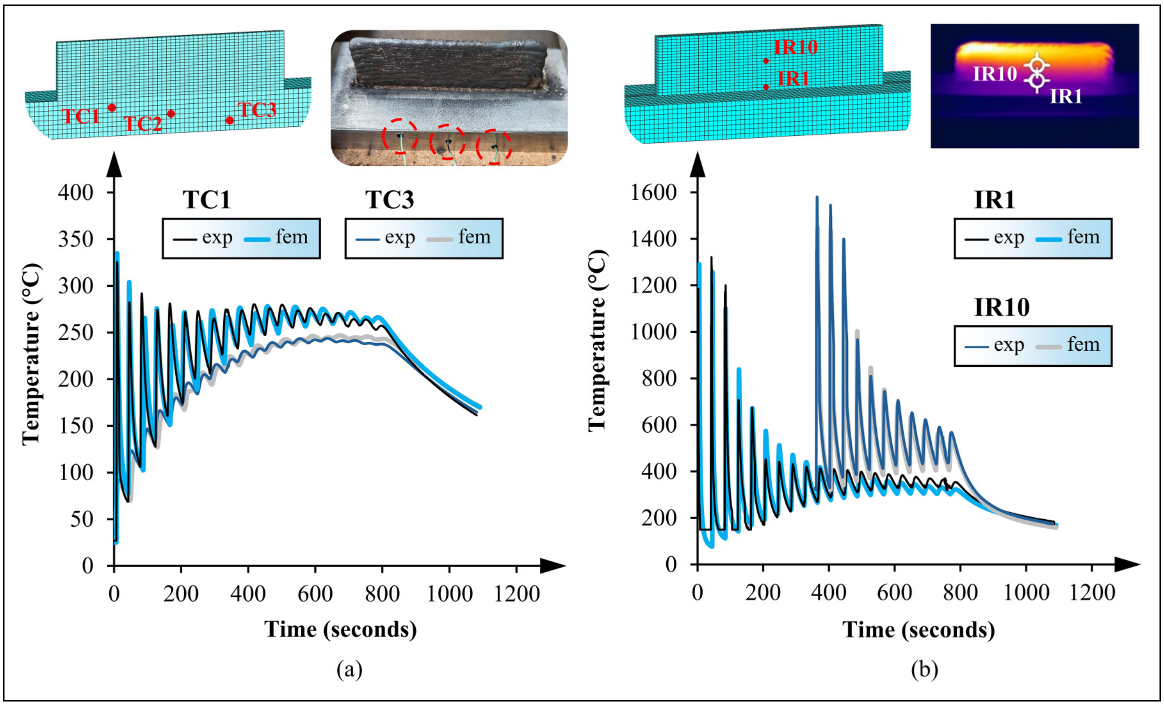

Figure 6. Finite element predicted and experimentally measured temperature evolutions over time for the thermocouples (a) TC1 and TC3 placed inside the baseplate and (b) IR1 and IR10 located on the wall surface, at the center of the first and tenth deposited layers.

numerically simulated by incorporating newborn elements into the existing finite element model.

The first temperature spike at IR10, occurring during the deposition of the tenth layer, further demonstrates the good agreement between experimental measurements and finite element predictions.

The maximum temperatures and the heating and cooling rates of IR1 and IR10 during the first spikes exceeded those of TC1 and TC3, due to the cooling effect provided by the baseplate. The subsequent temperature spikes observed for all the thermocouples over time are a direct result of reheating caused by the deposition of the different layers. This phenomenon is a key aspect of the deposition process and plays a significant role in the thermal stresses, distortion and microstructure of the deposited material.

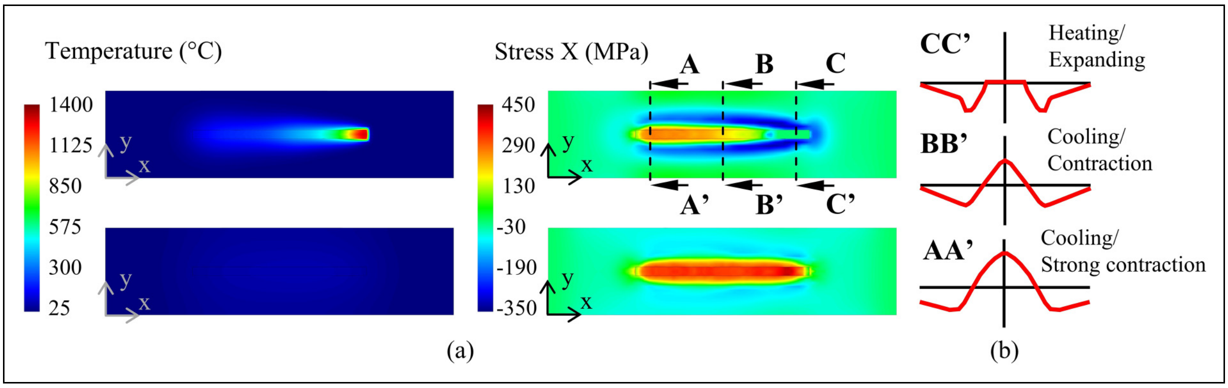

Figure 7. (a) Top-view of the finite element predicted distribution of longitudinal thermal stresses at the end of the first deposited layer with (b) the corresponding schematic plots at three different cross sections AA', BB' and CC'.

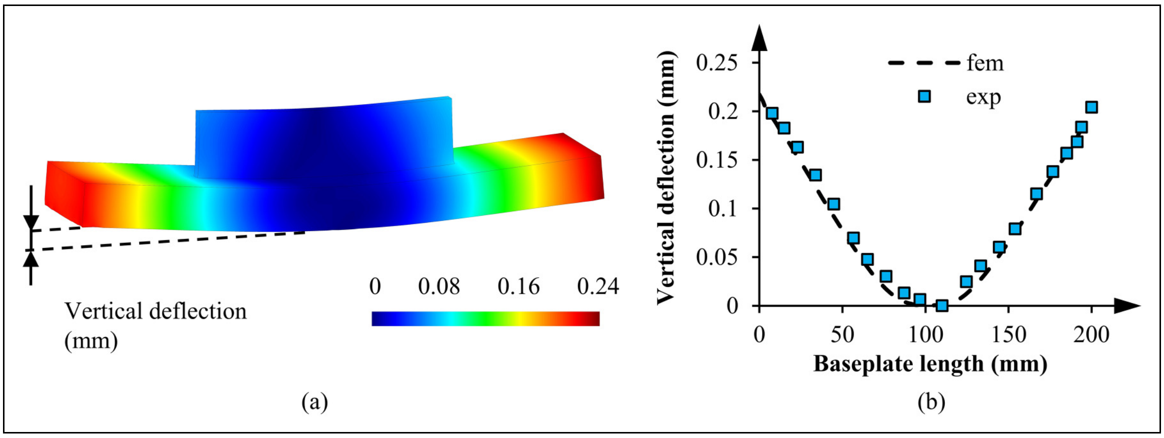

Figure 8. (a) Magnified finite element predicted distortion upon material cool down and removal of the clamps and (b) comparison between the predicted and measured profiles of the longitudinal edges of the bottom surface of the baseplate.

Thermal stresses and distortions

Thermal stresses result from differential thermal expansion and contraction of the deposited and baseplate materials during WAAM. Figure 7 provides a top view of the finite element model at the end of the deposition of the first layer, showing the predicted distribution of longitudinal thermal stresses.

Three main patterns are identified and summarized in the cross-sectional views depicted on the right-hand side of the figure. The first cross-section (labeled as AA') contains the molten pool with zero stresses and the neighboring heated region of the baseplate material with induced compression stresses. The latter is caused by the expansion of the neighboring heated baseplate material being restrained by the remaining material subjected to much lower temperatures.

The second cross-section (labelled as BB') is observed after some cooling of the deposited and neighboring heated baseplate materials. This results in tensile stresses because the shrinking of these two regions is restrained by the remaining baseplate material with lower temperatures. The third cross-section (labelled as CC') represents a time when the thermal contraction of the deposited and neighboring heated baseplate materials becomes more significant due to continued cooling. This leads to a further increase of the tension and compression thermal stresses.

Once the vertical wall and baseplate materials have cooled to ambient temperature and the clamps are removed, the residual stresses within the material lead to distortions. These distortions can be estimated by finite elements, as shown in the magnified plot of Figure 8(a), and excellent agreement is found between the computed and experimental profile of the longitudinal edges of the bottom surface of the baseplate, depicted in Figure 8(b). This result not only validates the finite element estimates of distortion but also indirectly validates the estimate of residual stresses.

Temperature gradients and microstructure

Figures 9(a) and 9(b) show the finite element computed distribution of the temperature gradient $\partial T / \partial x_j$ at the end of the deposition of the tenth layer and during cooling resulting from the waiting time of 30 s between deposition of the tenth and eleventh layers.

The temperature gradient is a crucial factor in understanding microstructure formation and was calculated at

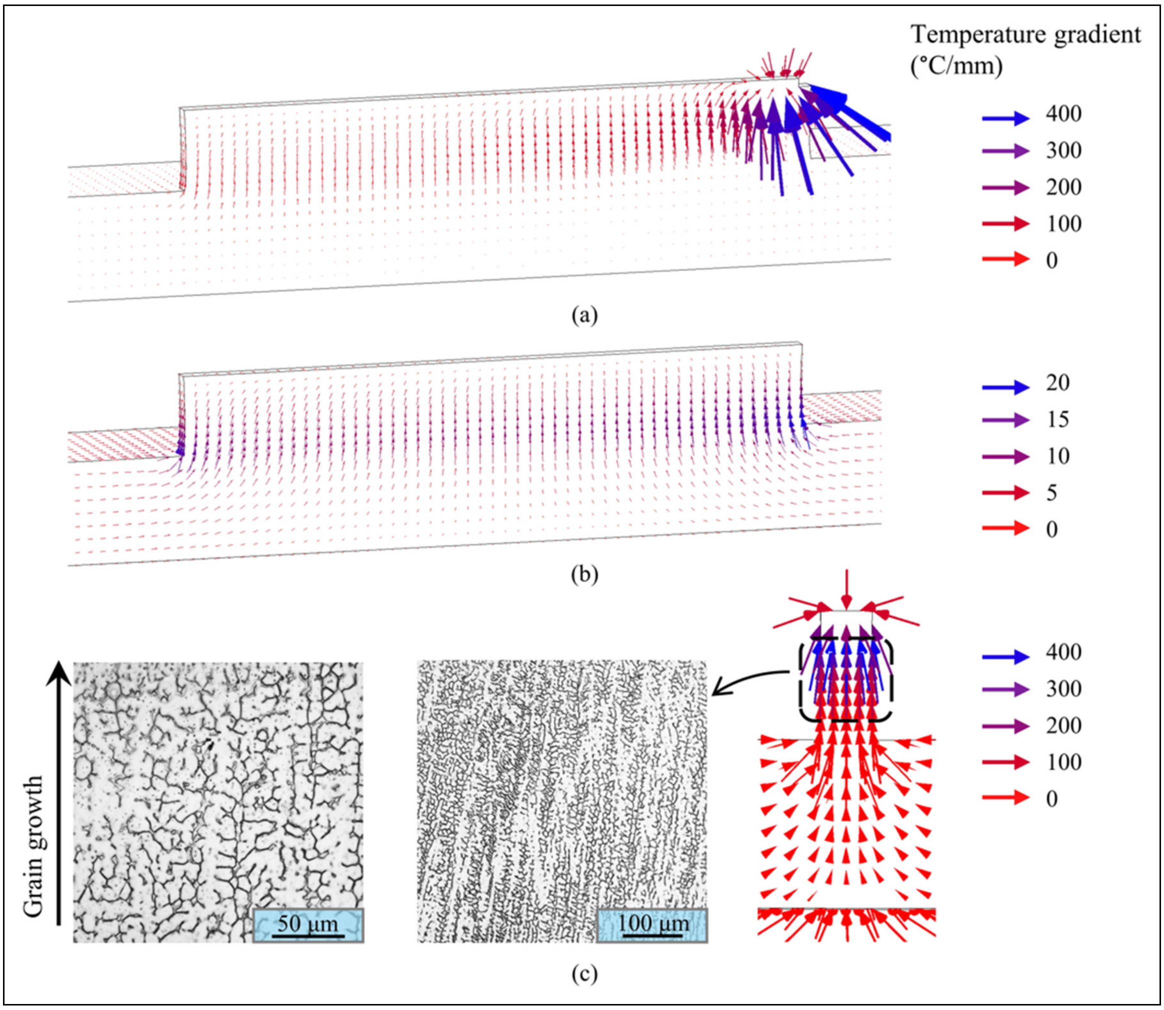

Figure 9. Finite element temperature gradient (a) at the end of the deposition of the tenth layer and (b) during cooling resulting from the waiting time of 30 s between deposition of the tenth and eleventh layers. (c) Microstructure observation of a sample extracted from the deposited wall with a cross section of the baseplate and wall showing the finite element temperature gradient.

the finite element level directly as $\mathbf{MT} = \nabla\mathbf{NT}$, where $\mathbf{N}$ denotes the matrix containing the shape functions, $\mathbf{M} = \nabla\mathbf{N}$ represents a matrix built from the gradient operator and $\mathbf{T}$ is the temperature at nodal point level. This innovative procedure supersedes determination of the temperature gradient $\partial T / \partial x_j$ from nodal temperature differences and distances between nodes within layers at the post-processing level, as commonly done by other researchers.[22]

Results depicted in Figure 9(a) and 9(b), reveal a significant concentration of the maximum temperature gradient at the right-hand side of the wall where material is being deposited. This concentration, however, becomes more uniform and aligned with the building height during the waiting time between consecutive layer depositions as the heat flows through the layers into the baseplate, as shown in Figure 9(b).

The alignment of the temperature gradient $\partial T / \partial x_j$ with the building height closely mirrors the orientation of the primary arms of dendritic growth (Figure 9(c)) and is a crucial factor in understanding the formation of columnar grain-based microstructures and their highly anisotropic behavior.

Conclusion

The in-house finite element software i-form was successfully extended to perform macro-scale thermo-mechanical modeling of WAAM. Results in single bead, multi-layer deposition of AISI 316L stainless steel along linear paths to create vertical walls show that the predicted temperature distributions agree well with the temperature measurements obtained by an infrared thermal camera, and the temperature evolutions over time in specific locations also agree well with experimental results obtained using thermocouples. Measurements in a coordinate measuring machine also confirm excellent agreement between the finite element predicted and measured baseplate distortion, indirectly validating residual stress estimates.

The proposed approach to computing the temperature gradient directly at the finite element level gave rise to results that closely mirror the orientation of the primary arm of dendritic growth and are in good agreement with microstructure observations.

Future work will be focused on the deposition of walls and structures other than linear.

Acknowledgments

The authors would like to acknowledge the support provided by Fundação para a Ciência e a Tecnologia (FCT) and IDMEC for its financial support via the project LAETA Base Funding (DOI: 10.54499/UIDB/50022/2020) and PTDC/EME-EME/0949/2020. Rui F.V. Sampaio would also like to acknowledge the support under the PhD Studentship 2022.12351.BD.

Declaration of conflicting interests

The authors declared no potential conflicts of interest with respect to the research, authorship, and/or publication of this article.

Funding

The authors disclosed receipt of the following financial support for the research, authorship, and/or publication of this article: This work was supported by the Fundação para a Ciência e a Tecnologia, (grant number DOI: 10.54499/UIDB/50022/2020 and PTDC/EME-EME/094, PhD Studentship 2022.12351.BD).

ORCID iDs

CV Nielsen https://orcid.org/0000-0001-7774-4399
PAF Martins https://orcid.org/0000-0002-2630-4593

References

1. Cunningham CR, Flynn JM, Shokrani A, et al. Invited review article: strategies and processes for high quality wire arc additive manufacturing. *Additive Manufacturing* 2018; 22: 672–686.
2. Montevecchi F, Venturini G, Scippa A, et al. Finite element modelling of wire-arc-additive-manufacturing process. *Procedia CIRP* 2016; 55: 109–114.
3. Cadiou S, Courtois M, Carin M, et al. Heat transfer, fluid flow and electromagnetic model of droplets generation and melt pool behaviour for wire arc additive manufacturing. *Int J Heat Mass Transfer* 2020; 148: 119102.
4. Hauser T, Reisch RT, Breese PP, et al. Porosity in wire arc additive manufacturing of aluminium alloys. *Additive Manufacturing* 2021; 41: 101993.
5. Liu CM, Gao HB, Li LY, et al. A review on metal additive manufacturing: modeling and application of numerical simulation for heat and mass transfer and microstructure evolution. *China Foundry* 2021; 18: 317–334.
6. Provatas N and Elder K. *Phase-field methods in materials science and engineering*. Weinheim, Germany: Wiley-VCH Verlag, 2010.
7. Yang H, Wu C, Li HW, et al. Review on cellular automata simulations of microstructure evolution during metal forming process: grain coarsening, recrystallization and phase transformation. *Science China Technological Sciences* 2011; 54: 2107–2118.
8. Lavery NP, Brown SGR, Sienz J, et al. A review of computational modelling of additive layer manufacturing – multiscale and multi-physics. In: *Proceedings of the International Conference on Sustainable Design and Manufacturing*, Cardiff, UK, 2014, pp.668–690.
9. Goldak JA and Akhlaghi M. *Computational welding mechanics*. New York: Springer, 2005.
10. Sampaio RFV, Pragana JPM, Bragança IMF, et al. Modelling of wire-arc additive manufacturing – A review. *Adv Ind Manuf Eng* 2023; 6: 100121.
11. Goldak J, Chakravarti A and Bibby MA. A new finite element model for welding heat sources. *Metall Trans B* 1984; 15B: 299–305.
12. Ding J, Colegrove P, Mehnen J, et al. A computationally efficient finite element model of wire and arc additive manufacture. *Int J Adv Manuf Technol* 2014; 70: 227–236.
13. Ling Y, Ni J, Abdel Wahab M, et al. A heat transfer finite element model for wire-arc-additive-manufacturing process. In: *Proceedings of the 8th International Conference on Fracture, Fatigue and Wear*, 2021, pp.201–215: Springer.
14. Nielsen CV and Martins PAF. Finite element flow formulation. In: *Metal forming: formability, simulation and tool design*. New York: Academic Press, Elsevier, 2021, pp.181–247.
15. Xiong J, Lei T and Li R. Finite element analysis and experimental validation of thermal behavior for thin-walled parts in GMAW-based additive manufacturing with various substrate preheating temperatures. *Appl Therm Eng* 2017; 126: 43–52.
16. Cambon C, Rouquette S, Bendaoud I, et al. Thermo-mechanical simulation of overlaid layers made with wire + arc additive manufacturing and GMAW-cold metal transfer. *Weld World* 2020; 64: 1427–1435.
17. Béraud N, Chergui A, Limousin M, et al. An indicator of porosity through simulation of melt pool volume in aluminum wire arc additive manufacturing. *Mechanics & Industry* 2022; 23: 1.
18. Chiumenti M, Cervera M, Salmi A, et al. Finite element modeling of multi-pass welding and shaped metal deposition processes. *Comput Methods Appl Mech Eng* 2010; 199: 2343–2239.
19. Pragana JP, Bragança IM, Reis L, et al. Formability of wire-arc deposited AISI 316L sheets for hybrid additive manufacturing applications. *Journal of Materials: Design and Applications* 2021; 235: 2839–2850.
20. Doege E, Meyer-Nolkemper H and Saeed I. *Fließkurvenatlas metallischer werkstoffe*. Munich: Hanser Verlag, 1986, pp.116–120.
21. The Engineering ToolBox, www.EngineeringToolBox.com (2024).
22. Yildiz AS, Koc B and Yilmaz O. Thermal behavior determination for wire arc additive manufacturing process. *Procedia Manufacturing* 2021; 54: 233–237.